

# Strain Modulation by van der Waals Coupling in Bilayer Transition Metal Dichalcogenide

Xiaoxu Zhao,<sup>†,‡,§</sup> Zijing Ding,<sup>†</sup> Jianyi Chen,<sup>†,¶</sup> Jiadong Dan,<sup>‡,§</sup> Sock Mui Poh,<sup>†,‡</sup> Wei Fu,<sup>†</sup> Stephen J. Pennycook,<sup>‡,§</sup> Wu Zhou,<sup>\*,†,⊥</sup> and Kian Ping Loh<sup>\*,†,¶</sup>

<sup>†</sup>Department of Chemistry and Centre for Advanced 2D Materials, National University of Singapore, 3 Science Drive 3, Singapore 117543

<sup>‡</sup>NUS Graduate School for Integrative Sciences and Engineering, National University of Singapore, 13 Centre for Life Sciences, #05-01, 28 Medical Drive, Singapore 117456,

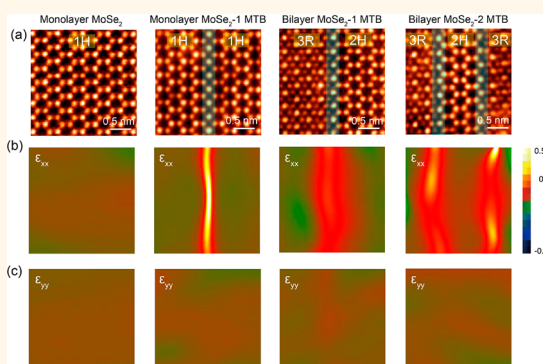
<sup>§</sup>Department of Materials Science and Engineering, National University of Singapore, Singapore 117575

<sup>¶</sup>School of Physical Sciences and CAS Center for Excellence in Topological Quantum Computation, University of Chinese Academy of Sciences, Beijing 100049, China

## Supporting Information

**ABSTRACT:** Manipulation of lattice strain is emerging as a powerful means to modify the properties of low-dimensional materials. Most approaches rely on external forces to induce strain, and the role of interlayer van der Waals (vdW) coupling in generating strain profiles in homobilayer transition metal dichalcogenide (TMDC) films is rarely considered. Here, by applying atomic-resolution electron microscopy and density functional theory calculations, we observed that a mirror twin boundary (MTB) modifies the interlayer vdW coupling in bilayer TMDC films, leading to the development of local strain for a few nanometers in the vicinity of the MTB. Interestingly, when a single MTB in one layer is “paired” with another MTB in an adjacent layer, interlayer-induced strain is reduced when the MTBs approach each other. Therefore, MTBs are not just 1D discontinuities; they can exert localized 2D strain on the adjacent lattices.

**KEYWORDS:** transition metal dichalcogenides, scanning transmission electron microscopy, strain engineering, van der Waals coupling, domain walls



Strain engineering has attracted tremendous interests over the past few years due to the promising prospect of modifying the properties of an atomically thin material by straining its lattice.<sup>1</sup> Strong charge-lattice coupling in 2D materials allows strain to modify a wide range of properties including optical,<sup>2–5</sup> electrical,<sup>6–8</sup> catalytic,<sup>9</sup> and magnetic<sup>10</sup> properties in group 6 transition metal dichalcogenides (TMDCs) ( $MX_2$ ,  $M = Mo$  or  $W$ ,  $X = S$  or  $Se$ ). For example, the band gap can be easily tuned by strain in 2D materials, including the direct-to-indirect band gap transition<sup>11,12</sup> and semiconducting-to-metal transition,<sup>13</sup> with related applications in broad-spectrum solar energy funnels<sup>5</sup> and piezotronics.<sup>14</sup> In most cases, the strain is introduced by extrinsic means,<sup>11–19</sup> whereas intrinsic lattice strain induced by the van der Waals (vdW) coupling in bilayer 2D materials is less explored. In bilayer graphene, it has been shown that strain solitons can form at stacking boundaries where the lattice stacking changes from AB to BA over a width of a few nanometers.<sup>15,16</sup> However, in homobilayer TMDC films, which have an elastic modulus much larger than that of graphene,<sup>1,17,18</sup> modulation of lattice

strain under the influence of interlayer vdW force has not been reported.

Here, employing combined atomic-resolution scanning transmission electron microscopy annular dark field (STEM-ADF) imaging and density functional theory (DFT) calculations, we discover that the strain profiles around mirror twin boundaries (MTBs) are strongly modulated by the vdW coupling in bilayer TMDCs. In a freestanding monolayer  $MoSe_2$  film containing a single MTB, denoted here as monolayer  $MoSe_2$ -1 MTB, both experiment and simulation reveal that the lattice strain induced by the MTB is confined within one unit cell on both sides of the MTB. In contrast, in a bilayer  $MoSe_2$  film containing a single MTB, denoted as bilayer  $MoSe_2$ -1 MTB, the strain field extends to ~3 nm around the MTB. The amount of lattice compression increases near the

Received: December 21, 2017

Accepted: January 31, 2018

Published: January 31, 2018

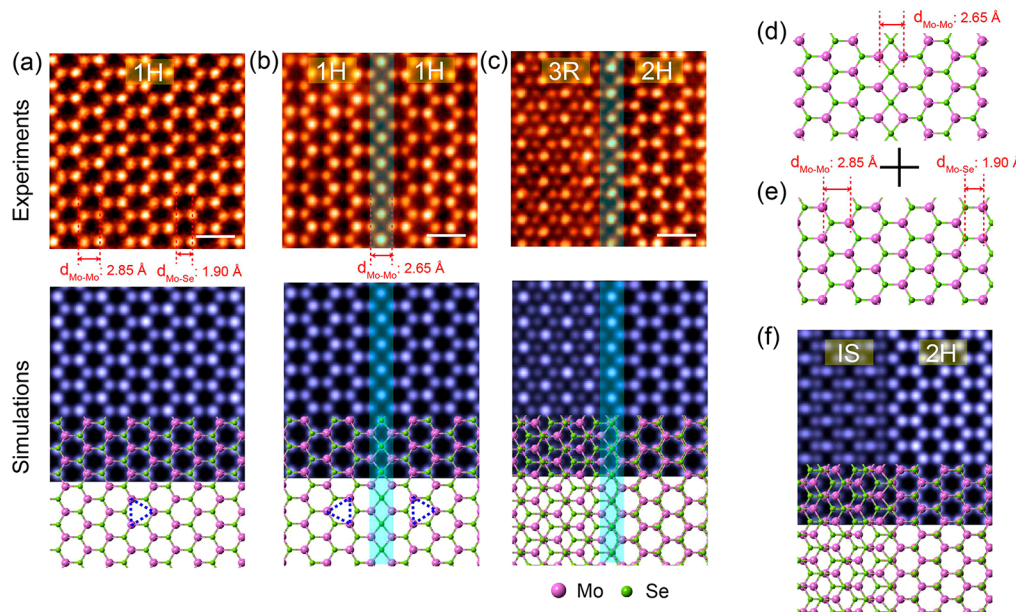


**Figure 1.** Electron microscopy study of the stacking registry evolutions in a bilayer MoSe<sub>2</sub> film in the presence of a MTB. (a–c) Atomic-resolution STEM-ADF images of (a) monolayer 1H MoSe<sub>2</sub>, (b) monolayer MoSe<sub>2</sub>-1 MTB, and (c) bilayer MoSe<sub>2</sub>-1 MTB films. Corresponding simulated images with overlaid DFT-optimized atomic models are depicted in the lower panels. MTBs are highlighted by cyan false color. (d,e) DFT-optimized atomic models of (d) a monolayer MoSe<sub>2</sub>-1 MTB film and (e) a monolayer 1H MoSe<sub>2</sub> film. (f) Simulated image of the unstrained bilayer MoSe<sub>2</sub>-1 MTB atomic model induced by manually stacking of a monolayer 1H MoSe<sub>2</sub> film and a monolayer MoSe<sub>2</sub>-1 MTB film without DFT relaxation. The atomic model of the unstrained bilayer MoSe<sub>2</sub>-1 MTB film is overlaid in the simulated image. Scale bars: 0.5 nm.

MTB, and the average strain of the entire 3 nm region is determined to be 1.6%. Similar phenomena have also been experimentally observed in bilayer MoS<sub>2</sub>-1 MTB and bilayer WSe<sub>2</sub>-1 MTB films. DFT calculations suggest that the delocalized strain profiles observed in bilayer TMDC-1 MTB films are due to interlayer vdW coupling, where the strong tendency to form low-energy bilayer stacking registries on both sides of the MTB imposes a gradual compression on the lattices near the MTB. On the other hand, when MTBs are present in both MoSe<sub>2</sub> layers in a bilayer film and are less than ~3 nm apart, hereafter denoted as bilayer MoSe<sub>2</sub>-2 MTB, the interlayer-induced strain is quenched, as confirmed both experimentally and theoretically.

## RESULTS AND DISCUSSION

**Distinct Strain Profiles in Monolayer and Bilayer MoSe<sub>2</sub>-1 MTB Films.** An atomic-resolution STEM-ADF image of a monolayer MoSe<sub>2</sub> film prepared by MBE (see Methods) is shown in Figure 1a and Figure S1. The measured average lattice constant is 3.29 Å, which is consistent with DFT calculations.<sup>12</sup> The projected nearest Mo–Se<sub>2</sub> distance ( $d_{\text{Mo–Se}}$ ) in the honeycomb is 1.90 Å (Figure 1a), which is taken as the reference unit length  $a$ . MTBs, particularly the 4I4P-type<sup>19</sup> containing four-fold rings that share points at Se dimer sites, are commonly observed in monolayer (Figure 1b) and bilayer (Figure 1c) MoSe<sub>2</sub> films.<sup>20</sup> Although theoretical calculations<sup>21</sup> suggest that there are potentially more than 10 types of MTBs in TMDC films, the 4I4P MTB is the predominant structure observed in synthetic<sup>19,22,23</sup> MoSe<sub>2</sub> crystals, whereas the 4I4E (edge-sharing)-type MTB is often observed under e-beam irradiation.<sup>22,23</sup>

In the monolayer MoSe<sub>2</sub>-1 MTB film (Figure 1b), the presence of the MTB separates the film into two mirror symmetric grains,<sup>22,23</sup> as highlighted in the atomic model.

Consequently, when a monolayer MoSe<sub>2</sub>-1 MTB structure is stacked onto a perfect monolayer without MTB, as in the case of a bilayer MoSe<sub>2</sub>-1 MTB film, two distinct types of bilayer stacking registries form on each side of the MTB. As shown in Figure 1c, the stacking registries in the bilayer film separated by the MTB are 3R (AB) and 2H (AA'), which are commonly observed in our experiments. In order to transform from 2H to 3R bilayer stacking, one of the monolayers has to undergo a mirror symmetry operation plus a relative in-plane displacement  $\mu$ , which is equal to the unit length  $a$  (1.90 Å), along the armchair direction. Notice that in a freestanding monolayer, the MTB not only imposes a mirror symmetry operation on the lattice but also induces an in-plane displacement due to the presence of four-membered rings. However, the in-plane Mo–Mo distance ( $d_{\text{Mo–Mo}}$ ) in the MTB in a freestanding monolayer is 2.655 Å, that is, ~75 pm larger than what is needed for a perfect 2H to 3R transition. To illustrate this point, we simulated a freestanding monolayer MoSe<sub>2</sub>-1 MTB film (Figure 1d) stacked onto a perfect 1H-MoSe<sub>2</sub> monolayer (Figure 1e) without lattice relaxation. As shown in Figure 1f, when one side of the MTB forms perfect 2H stacking, the other side of the MTB deviates considerably from the perfect 3R registry and forms instead an intermediate state. The intermediate state (IS) is evolved from the 3R registry by the gliding of one layer against the other along the Mo zigzag direction for 75 pm ( $\Delta\mu = 75$  pm), which is equivalent to the additional in-plane displacement imposed by the four-membered rings in the MTB (see Supplementary section 1 for a detailed discussion). In other words, in order to form the 2H|3R stacking registries across the MTB as observed experimentally (Figure 1c), the lattice of the monolayer containing the MTB must be strained in order to accommodate the 75 pm in-plane displacement difference.

To further analyze the strain profile differences in a bilayer MoSe<sub>2</sub>-1 MTB film and monolayer MoSe<sub>2</sub>-1 MTB film, geometric phase analysis<sup>24</sup> was applied. This allows any lattice distortions to be qualitatively spotted. By comparing the strain components  $\varepsilon_{xx}$  and  $\varepsilon_{yy}$ , we can immediately identify whether the strain is normal strain ( $\Delta\mu$  perpendicular to the MTB), shear strain ( $\Delta\mu$  parallel to the MTB), or combined. It is observed that the strain component  $\varepsilon_{xx}$  in a monolayer MoSe<sub>2</sub>-1 MTB film (Figure S2) is concentrated along the MTB region and only affects the lattices for one unit length normal to the MTB, and this observation is supported by both experimental and theoretical results discussed later. On the other hand, the strain profile of  $\varepsilon_{xx}$  in a bilayer MoSe<sub>2</sub>-1 MTB film (Figures S1 and S2) is delocalized into the adjacent lattice regions for over ~1 nm. More regions showing similar strain delocalization processes in bilayer MoSe<sub>2</sub>-1 MTB films are depicted in Figure S4. In addition, mono- and bilayer MoSe<sub>2</sub>-1 MTB films reveal abundant  $\varepsilon_{xx}$  strain, whereas it is almost strain free along  $\varepsilon_{yy}$  (Figure S2), indicating that the exerted strain is predominantly perpendicular to the MTBs.

The interlayer coupling-induced strain effects we observed are not only restricted to MoSe<sub>2</sub>. We have verified that the presence of MTBs in bilayer WSe<sub>2</sub> and MoS<sub>2</sub> also imposes in-plane displacements going across the MTB from the 2H to 3R stacking, with  $\Delta\mu = \sim 76$  pm in WSe<sub>2</sub> and  $\Delta\mu = \sim 78$  pm in MoS<sub>2</sub> (Table S1). Delocalized strain profiles are consistently observed in bilayer WSe<sub>2</sub>-1 MTB (Figure S6) and MoS<sub>2</sub>-1 MTB films (Figure S5). Clear stacking transitions from the intermediate state to 3R or 2H have been experimentally observed, confirming the presence of the strain gradients. Therefore, we conclude that the delocalized strain profiles in the vicinity of the MTB as induced by the modified interlayer vdW coupling are common in bilayer group 6 TMDC films.

**Quantitative Strain Analysis in a Bilayer MoSe<sub>2</sub>-1 MTB Film.** To observe the spatial distribution of lattice strain induced by the interlayer vdW coupling, STEM-ADF imaging was performed on both monolayer MoSe<sub>2</sub>-1 MTB film (which has no interlayer vdW coupling) and bilayer MoSe<sub>2</sub>-1 MTB film to compare their lattice distortion at each atomic site. First, we carried out image simulations to evaluate the strain quantification in 3R-stacked regions (Figure 2). In a 3R-stacked bilayer MoSe<sub>2</sub> film, there are three distinct atom sites (*i.e.*, Mo, Se<sub>2</sub>, and Mo + Se<sub>2</sub>) in each honeycomb. The Mo and Se<sub>2</sub> atom sites belong to the top and bottom layers, respectively. Lattice strain imposed on the MTB-containing layer is reflected by the projected length (between Mo and Mo + Se<sub>2</sub> sites, denoted as  $d_{\text{Mo-MoSe}_2}$ ) variations, as highlighted by the red dashed lines (Figure 2). The strain-free unit length  $a$  (*i.e.*,  $d_{\text{Mo-Se}}$  of 1.9 Å) is observed in a monolayer MoSe<sub>2</sub>-1 MTB film (see Supplementary section 2 for a detailed discussion). When the MTB-containing layer in bilayer 3R-stacked models is subjected to increasing degree of strain, that is, ranging from 0 to 70 pm (Figure 2a–g), the projected  $d_{\text{Mo-MoSe}_2}$  distances in the corresponding simulated STEM-ADF images are increasingly reduced from the strain-free value of 1.9 Å (Figure 2a–f) and reaches 1.2 Å at the highest strain applied (Figure 2g). Therefore, the experimental lattice strain exerted in the MTB layer can be quantified by comparing the  $d_{\text{Mo-MoSe}_2}$  in each honeycomb.

In a typical STEM-ADF image of a bilayer MoSe<sub>2</sub>-1 MTB film (Figure 3a), atoms in the top MTB layer are highlighted by the yellow false color, and atoms in the bottom 1H layer are

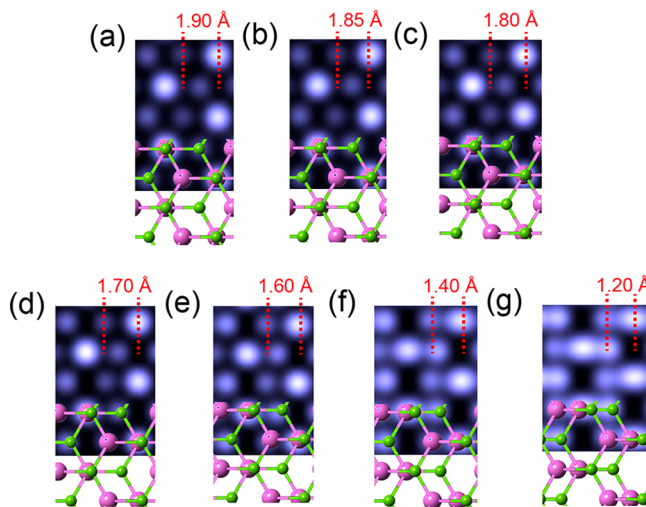


**Figure 2.** Strain quantification in bilayer MoSe<sub>2</sub> films by the image simulation. (a–g) Simulated images with increasing degree of strain: 0 pm (a), 5 pm (b), 10 pm (c), 20 pm (d), 30 pm (e), 50 pm (f), and 70 pm (g) in 3R-stacked bilayer MoSe<sub>2</sub> films. The corresponding atomic models are overlaid with the simulated images.

highlighted by the cyan false color. It can be seen that in the bilayer MoSe<sub>2</sub>-1 MTB film, the  $d_{\text{Mo-Se}}$  distance (Figure 3b) in the MTB plane gradually increases from 1.4 Å ( $\Delta\mu = 50$  pm) at column 1 to 1.9 Å ( $\Delta\mu = 0$ ) at column 12, suggesting that strain is continuously absorbed by the proximal lattices, and ~75 pm in-plane displacements are fully accommodated from column 12 onward (red curve in Figure 3c). In the enlarged STEM images (Figure 3b), it can be seen that in the bilayer MoSe<sub>2</sub>-1 MTB film, most strain is absorbed by the lattices adjacent to the MTB, in which the nearest three honeycombs (~8.6 Å) accommodate ~30 pm (~3.5% compressive strain) while the outer eight honeycombs (~22.8 Å) only absorb ~20 pm (~0.9% compressive strain). The average lattice distortion in the entire 3R-stacked region is calculated to be ~1.6%. The strain exerted on the four-membered ring of the MTB is ~15 pm, which is calculated by comparing the  $d_{\text{Mo-Mo}}$  distance (at column 0, ~2.5 Å) with the corresponding  $d_{\text{Mo-Mo}}$  value (~2.65 Å) in a monolayer MoSe<sub>2</sub>-1 MTB film (blue curve in Figure 3c). Unlike the layer containing the MTB in bilayer MoSe<sub>2</sub>-1 MTB film, the layer without MTB in the bilayer is largely strain free and has a fully relaxed  $d_{\text{Mo-Se}}$  value (Figure S3) similar to that of monolayer MoSe<sub>2</sub>-1 MTB film (blue curve in Figure 3c) without interlayer vdW coupling. The latter has a fully relaxed  $d_{\text{Mo-Se}}$  value of 1.9 Å at column 2 onward (the STEM image used is shown in Figure S1). Therefore, our results suggest that interlayer vdW forces coupled to MTBs delocalize the strain beyond the range of the local disorder.

**Quenching of Interlayer Strain in Bilayer MoSe<sub>2</sub>-2 MTB Films.** When bilayer MoSe<sub>2</sub> films were grown at a lower temperature (see Methods), a higher density of paired MTBs appeared, where one MTB in the upper layer is “paired” with a second in the lower layer. As shown in Figure 4, the presence of an intermediate state (IS) between the two MTBs results in a unique 3R|IS|3R lateral hybrid structure, and the size of the intervening IS regions increases linearly with the separation distance between the two MTBs (Figure 4a–d). Interestingly, the in-plane displacement caused by the top MTB and the bottom MTB with respect to the 3R regions cancel each other

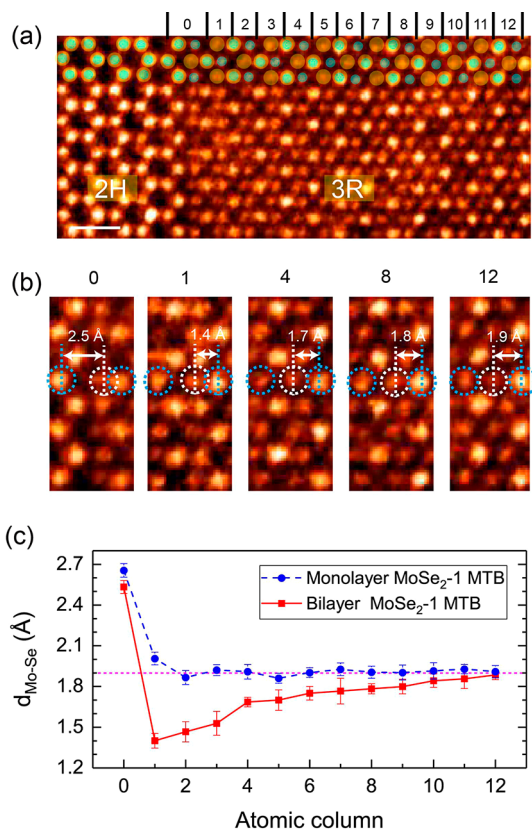


**Figure 3.** Quantitative strain analysis in a bilayer MoSe<sub>2</sub>-1 MTB film. (a) Atomic-resolution STEM-ADF image showing a 2H|3R domain boundary in a bilayer MoSe<sub>2</sub>-1 MTB film. (b) Enlarged images at atomic columns 0, 1, 4, 8, and 12, showing the strain relaxation process. (c) Measured  $d_{\text{Mo-Se}}$ , i.e., unit length  $a$ , at each honeycomb in the MTB layer in the bilayer MoSe<sub>2</sub>-1 MTB film (red curve) and monolayer MoSe<sub>2</sub>-1 MTB film (blue curve). The STEM-ADF image used for calculating the unit length  $a$  in the monolayer MoSe<sub>2</sub>-1 MTB film is shown in Figure S1. The unstrained unit length  $a$  (1.90 Å) is highlighted by the cyan dashed line. Scale bar: 0.5 nm.

( $\Delta\mu = 0$ ), thereby the driving force for generating interlayer-induced strain at 3R regions is annihilated. To quantitatively verify the quenching of interlayer-induced strain in bilayer MoSe<sub>2</sub>-2 MTB films, the unit length  $a$  of each honeycomb lattice in both layers is systematically calculated when the separation distance between two MTBs are 0.5a, 1a, 2a, and 2.5a, and the results are shown in Figure 4e–h. It can be seen that the unit length  $a$  adjacent to the MTB in all bilayer MoSe<sub>2</sub>-2 MTB films is similar to the unstrained value (i.e., 1.9 Å), as highlighted by the cyan dashed lines. Delocalized strain profiles displayed in the bilayer MoSe<sub>2</sub>-1 MTB film are not present in any of the bilayer MoSe<sub>2</sub>-2 MTB films, and all Mo atoms locate right at the center of each honeycomb in all 3R-stacked regions (Figure S7). In addition, simulated images (Figure 4) derived from the DFT-optimized models of bilayer MoSe<sub>2</sub>-2 MTB films with various separation distances agree well with the experimental images at all atomic positions. Importantly, the DFT-calculated unit length  $a$  in all honeycombs (Figure 4) of bilayer MoSe<sub>2</sub>-2 MTB films is equivalent to that of the monolayer MoSe<sub>2</sub>-1 MTB film (Figure 7f), which indicates the absence of interlayer-induced strain. This provides clear evidence that the strain induced by interlayer vdW coupling

is quenched when two MTBs couple to each other in bilayer MoSe<sub>2</sub> films.

### Lateral Hybrid Structures in Bilayer MoSe<sub>2</sub>-2 MTB Films.

The presence of two MTBs in bilayer MoSe<sub>2</sub> films sandwiching an intervening area gives rise to a ternary phase, lateral hybrid structure. In a bilayer MoSe<sub>2</sub>-1 MTB film, the most commonly observed domain boundary is 3R|2H; going across this boundary gives a symmetry transition from centrosymmetric (2H) to noncentrosymmetric (3R). When the bilayer film contains two MTBs (one on each layer) with separation distances of 2a, 3.5a, 5a, and 6.5a, a lateral hybrid interface of 3R|2H|3R, which involves double symmetry breaking, is generated, as is confirmed by the STEM-ADF imaging and image simulation (Figure 5). In addition, a 3R'|3R domain boundary (Figure S8) displaying a similar symmetry transition from centrosymmetric (3R') (Figure S9) to noncentrosymmetric (3R) structure is occasionally observed in bilayer MoSe<sub>2</sub>-1 MTB films. A 3R'|3R domain boundary can evolve from a 2H|3R domain boundary by translating the bottom 1H layer a unit length  $a$  along the Mo zigzag direction (see Supplementary section 3 for a detailed discussion). When the two MTBs are separated by 4a or 5.5a, a 3R|3R'|3R lateral hybrid is formed instead (Figure 6), as evidenced by STEM and image simulation. Therefore, by manipulating the separation distance between two MTBs, a diverse range of symmetry breaking can be introduced, which raises the interesting prospect of applying a bilayer MoSe<sub>2</sub>-2 MTB film as a valley filter.<sup>25–27</sup>

**DFT Calculations.** DFT calculations were carried out to provide insights into the strain profiles in mono- and bilayer MoSe<sub>2</sub> films. First, the relative stabilities of various stacking registries in bilayer MoSe<sub>2</sub> films are calculated by translating one MoSe<sub>2</sub> layer over the other along the zigzag direction (Figure 7a,b). Two categories of stacking registries, that is, two layers oriented in opposite crystallographic direction (Figure 7a) and two layers oriented in the same crystallographic direction (Figure 7b), are calculated. Evidently, the 3R (AB) and 2H (AA') stacking registries located at the valley points are the most stable configurations when two layers orient in either the opposite or the same crystallographic direction, respectively. There is a thermodynamic driving force to form low-energy bilayer stacking registries in bilayer MoSe<sub>2</sub> films, as suggested by the energy landscape (Figure 7a,b). The binding energy of 2H stacking is calculated to be 25.4 meV/Å<sup>2</sup>.<sup>28</sup> The 2H stacking registry, being the most thermodynamically stable phase, is set as zero energy, and all the energies of other stacking types are normalized against it.

To investigate the energetics of the monolayer or bilayer system containing MTBs, DFT (see Methods) calculations were performed (Figure 7c–e). To eliminate the edge effect, all MoSe<sub>2</sub> models (Figure 7c–e) we built are 64 Å long, that is,  $14\sqrt{3} \times 1$  unit cell. After DFT optimization (see Methods) of bilayer atomic models containing either single or double MTBs (Figure 7d,e), the interlayer-induced strain is calculated by comparing the variations in unit length  $a$  in each honeycomb to the corresponding value in the DFT-optimized monolayer MoSe<sub>2</sub>-1 MTB model (Figure 7c). The calculated strain profiles are depicted in Figure 7f. Notably, lattice distortions, which reflect the presence of interlayer vdW coupling, are observed in the bilayer MoSe<sub>2</sub>-1 MTB film (black dots in Figure 7f); this is caused by the interlayer in-plane displacement imposed by the MTB. The delocalization of the strain within a length scale of a few nanometers can be understood by the competition between

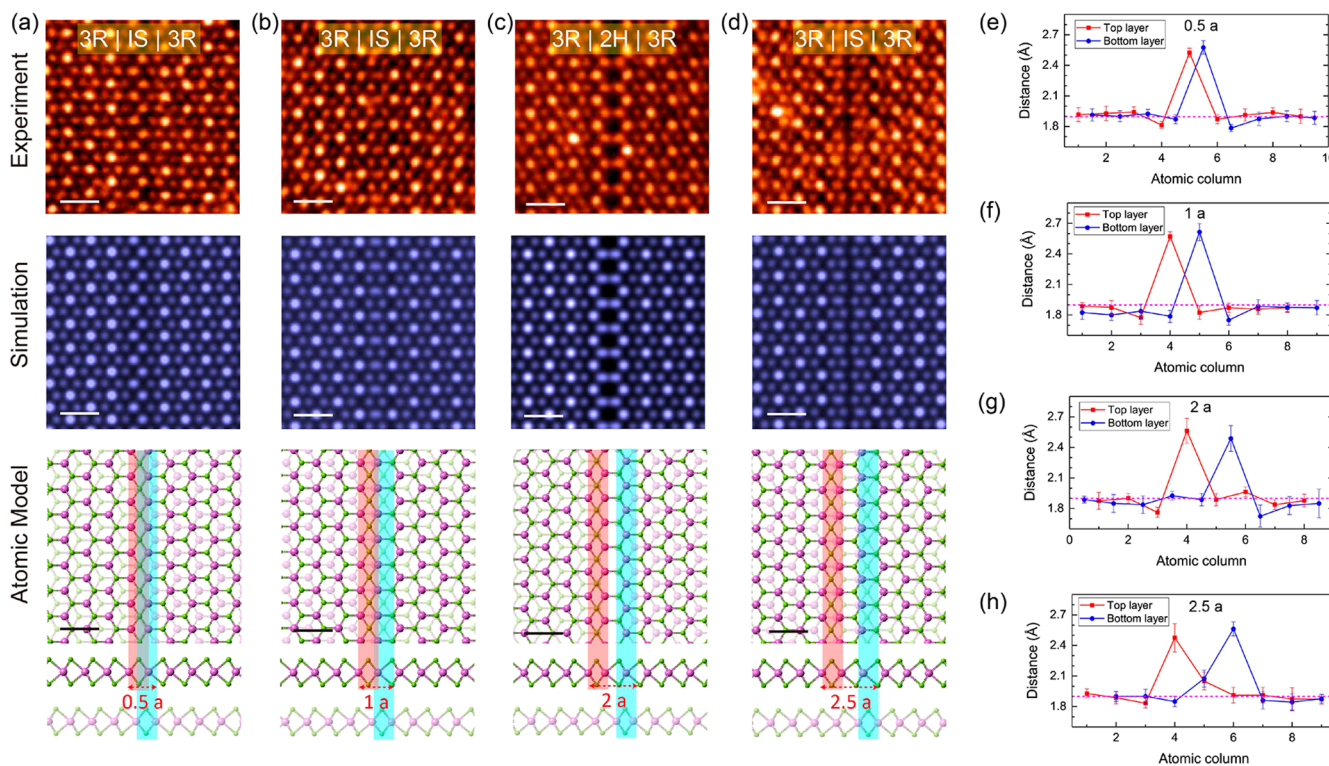
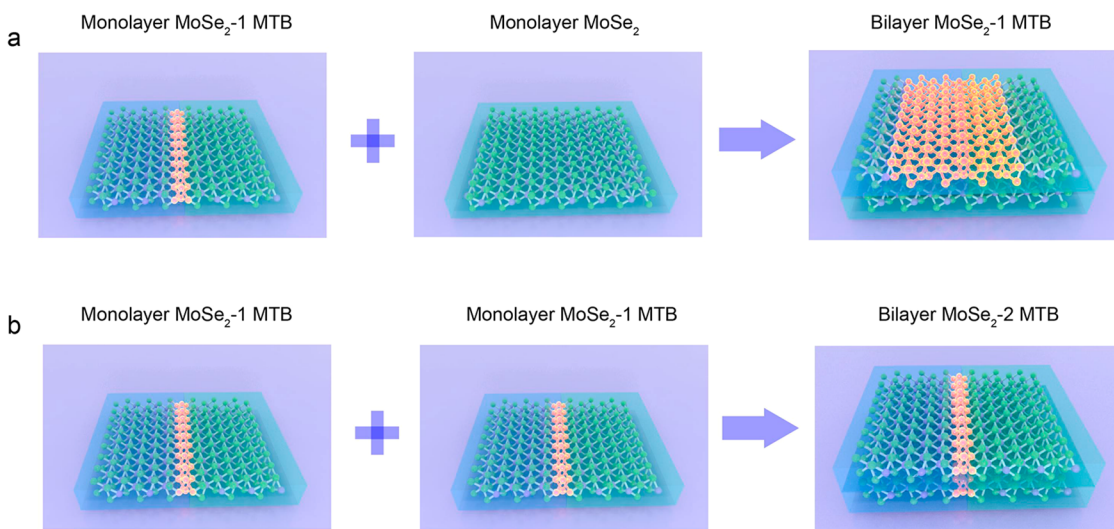


**Figure 4.** Electron microscopy study of the strain distribution in bilayer MoSe<sub>2</sub>-2 MTB films. (a–d) Atomic-resolution STEM-ADF images showing 3R|IS|3R domain boundaries in bilayer MoSe<sub>2</sub>-2 MTB films, where the separation distance between two MTBs are (a) 0.5a, (b) 1a, (c) 2a, and (d) 2.5a. Corresponding simulated images and DFT-optimized atomic models are displayed in the lower panels. MTBs located at the top and bottom layers are highlighted by the red and cyan false colors, respectively, in the atomic models. (e–h) Measured unit length  $a$  in top (red) and bottom (blue) layers at each atomic column in bilayer MoSe<sub>2</sub>-2 MTB films shown in (a–d). The unstrained unit length  $a$ , i.e., 1.9 Å, is highlighted by the cyan dashed lines. The saddle point in each curve is the  $d_{\text{Mo-Mo}}$  distance in the four-membered ring in the MTB. Scale bars: 0.5 nm.

**Scheme 1. Schematic Illustration of Strain Distributions in (a) Bilayer MoSe<sub>2</sub>-1 MTB and (b) Bilayer MoSe<sub>2</sub>-2 MTB Films (Strained Lattices Are Highlighted by the Yellow False Color)**



the strain energy in the bilayer lattice and the misalignment energy cost of interlayer vdW forces. Interestingly large strain is distributed near the MTB region (black dots in Figure 7f), and the strain gradient exists at a distance normal to the MTB for a length of ~2 nm, which is consistent with experimental results (Figure 2). The bottom pristine 1H layer in bilayer MoSe<sub>2</sub>-1 MTB film, however, is almost unaffected (Figure S3a), which is

consistent with our experimental result (see **Supplementary section 4** for a detailed discussion).

In addition to acting as a compressive strain boundary, the MTB can also serve as a shear strain boundary when domains become translated by fractional lattice constants. MoSe<sub>2</sub> lattices that are shear strained ( $\Delta\mu$  is parallel to the boundary) produce other stacking registries (N-stacking), as depicted in Figure

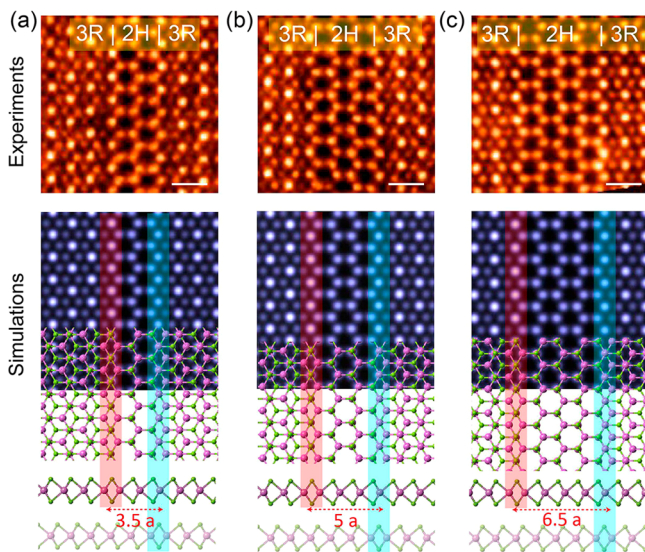


**Figure 5.** Domain boundaries revealing 3R|2H|3R lateral hybrid structures in bilayer MoSe<sub>2</sub>-2 MTB films with increasing separation distances. (a–c) Atomic-resolution STEM-ADF images of bilayer MoSe<sub>2</sub>-2 MTB films showing 3R|2H|3R lateral hybrid structures. The separation distances between the two MTBs are 3.5a (a), 5a (b), and 6.5a (c). Corresponding simulated images with the overlaid atomic models are displayed in the lower panels. The side views of all the atomic models are provided below. MTBs located at the top and bottom layers are highlighted by red and cyan false colors in the atomic models, respectively. Scale bars: 0.5 nm.

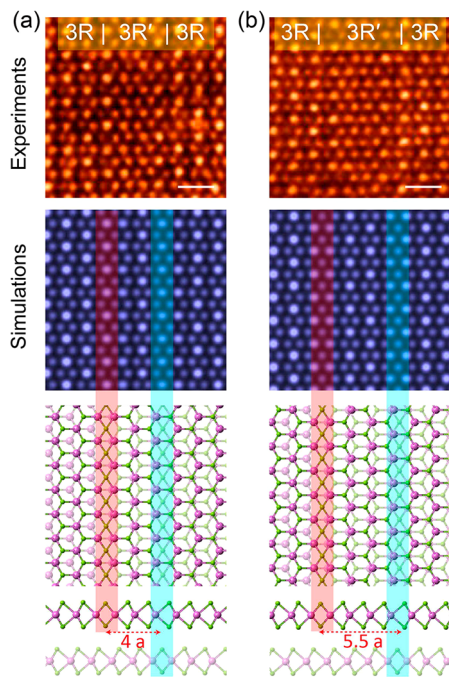


**Figure 6.** Domain boundaries revealing 3R|3R'|3R lateral hybrid structures in bilayer MoSe<sub>2</sub>-2 MTB films with increasing separation distances. (a,b) Atomic-resolution STEM-ADF images of bilayer MoSe<sub>2</sub>-2 MTB films showing 3R|3R'|3R lateral hybrid structures. The separation distances between the two MTBs are 4a (a) and 5.5a (b). Corresponding simulated images with the overlaid atomic models are displayed in the lower panels. The side views of all the atomic models are provided below. MTBs located at the top and bottom layers are highlighted by red and cyan false colors in the atomic models, respectively. Scale bars: 0.5 nm.

S12a, which match well with the simulated image (Figure S12b) derived from the DFT-optimized model. The Mo atoms at N-stacked regions undergo relative gliding with respect to the corresponding Mo atoms in monolayer MoSe-1 MTB film in both X and Y directions (Figure S12c). In addition, lattice strain developed along directions parallel and perpendicular to the MTB are also confirmed by strain mapping (Figure S13).

## CONCLUSIONS

In conclusion, we have investigated the strain profiles in bilayer homo-TMDC films containing either single MTB or double MTBs. For a bilayer film containing a single MTB, interlayer strain is commonly observed in a wide class of TMDCs (e.g., MoSe<sub>2</sub>, WSe<sub>2</sub>, and MoS<sub>2</sub>), whereby the MTBs divide the crystals into 3R and 2H phases. An average 1.6% lattice strain has been determined in the 3R domains in a bilayer MoSe<sub>2</sub>-1 MTB film over a distance of ~3 nm (11 honeycombs) from the MTB, which should impact the local conductance and thermoelectric properties.<sup>11,12</sup> The delocalization of the strain in the bilayer system, however, is quenched by the presence of “paired” MTBs when they are within interacting distance, which implies that there is a tendency for MTBs to move towards each other if the activation barrier for grain boundary diffusion can be surmounted. Recently, the formation of a high density of MTBs has been successfully demonstrated in MoSe<sub>2</sub>;<sup>29</sup> therefore, understanding interlayer interactions in the presence of MTBs potentially affords alternative routes for strain engineering of layered structures.

## METHODS

**Growth of TMDC Bilayer Films.** *MBE-Grown MoSe<sub>2</sub> Films.* MoSe<sub>2</sub> bilayer films were grown in a dedicated MBE chamber (base pressure <6 × 10<sup>-10</sup> Torr). Prior to the growth, the SiO<sub>2</sub> substrates were degassed in the same chamber for 1 h and annealed at 500 °C for 10 min. Mo and Se powders were evaporated from an electron-beam evaporator and a Kunksen cell, respectively. During growth, the temperature of the SiO<sub>2</sub> substrates was maintained at 500 °C, with a flux ratio between Mo and Se of ~1:10 and chamber pressure kept at ~9 × 10<sup>-10</sup> Torr. An ultrahigh density of MTBs in bilayer MoSe<sub>2</sub> can be achieved when the growth temperature is set at 250 °C.

**Chemical Vapor Deposition (CVD)-Grown MoS<sub>2</sub> and WSe<sub>2</sub> Films.** MoS<sub>2</sub> crystals were grown on a piece of molten soda-lime-silica glass substrate. Prior to growth, the glass substrates were sequentially cleaned by acetone, isopropyl alcohol (IPA), and deionized water following by a 5 min O<sub>2</sub> plasma treatment. A piece of 285 nm thick SiO<sub>2</sub>/Si substrate with a piece of Mo foil on the surface was used as a supporting substrate placed just beneath the glass. A small amount of Mo precursors (~1 mg MoO<sub>3</sub> powders) was sandwiched between the supporting substrates, and another piece of SiO<sub>2</sub>/Si substrate was placed just above the heating zone of the furnace. The detailed configuration can be seen in ref 30. S precursors (~0.8 g of sulfur powder) were loaded upstream in a quartz test tube. Ar gas (20 sccm) was used as the carrier gas. H<sub>2</sub> (3 sccm) was introduced to the CVD system. The growth temperature was set at ~1050 °C, and the growth time was ~5 min. The temperature of the S precursor was maintained at ~280 °C during the growth. The furnace was quickly cooled under a flow of Ar (200 sccm) after growth. WSe<sub>2</sub> crystals were grown by a method similar to that of MoS<sub>2</sub>. Se powder and WO<sub>3</sub> were used for growing WSe<sub>2</sub> crystals. The temperature of the Se precursors was maintained at ~280 °C during the growth. The difference is that a small quantity of H<sub>2</sub> (5 sccm) was required to enhance the selenization reaction of WO<sub>3</sub> during the growth of WSe<sub>2</sub> crystals.

**STEM Sample Preparation and Characterization.** *Sample Transfer.* As-grown TMDC bilayer films were identified by optical microscopy. Cu quanti-foil TEM grids were placed onto the targeted TMDC crystals followed by a IPA-assisted polymer-free transfer.<sup>31</sup> All

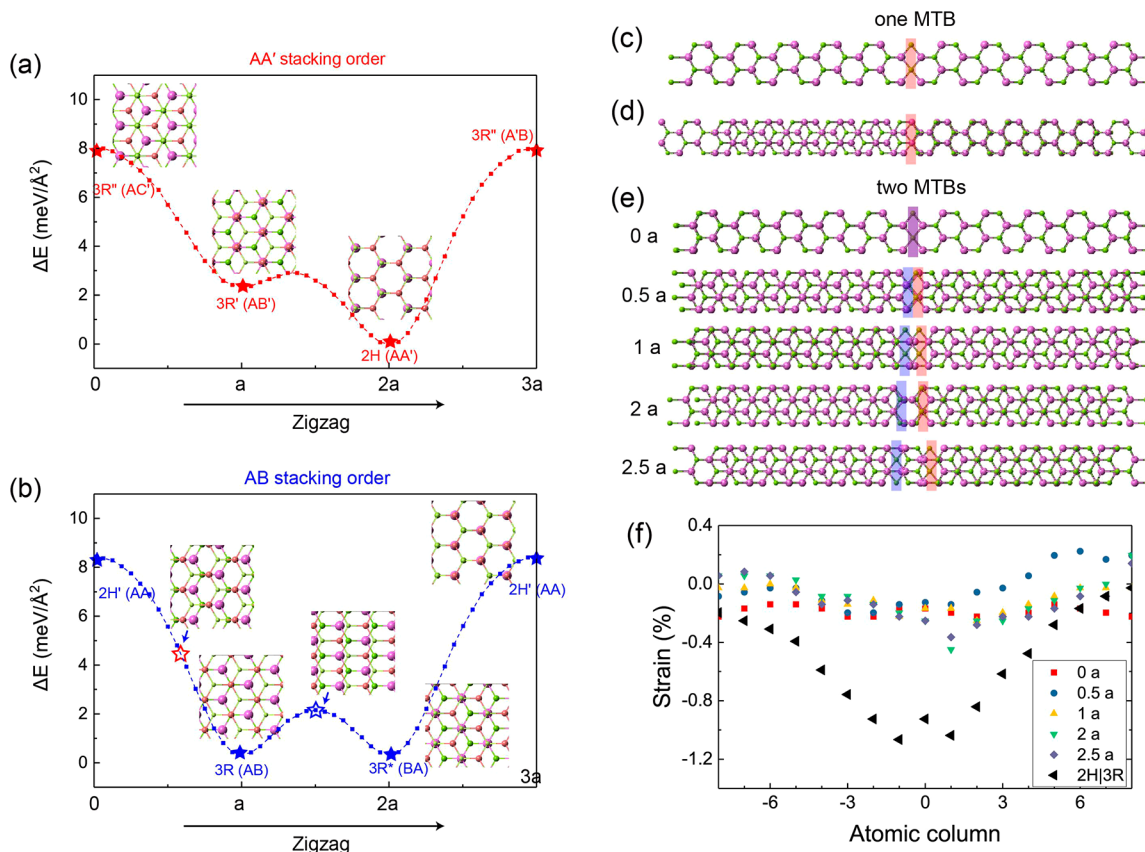


**Figure 7.** DFT-calculated strain profiles in homobilayer MoSe<sub>2</sub> films containing either a single or double MTB. (a,b) Energy landscapes for translating one MoSe<sub>2</sub> layer across the other along the zigzag direction in a bilayer MoSe<sub>2</sub> film. (a) Two MoSe<sub>2</sub> layers sharing the same crystal orientation and (b) two layers exhibiting 60° in-plane rotation. (c,d) DFT-optimized atomic models of (c) a monolayer MoSe<sub>2</sub>-1 MTB film and (d) a bilayer MoSe<sub>2</sub>-1 MTB film. (e) DFT-optimized atomic models of bilayer MoSe<sub>2</sub>-2 MTB films where the separation distances are 0, 0.5a, 1a, 2a, and 2.5a. (f) Calculated strain profiles in bilayer MoSe<sub>2</sub>-1 MTB films (d) and bilayer MoSe<sub>2</sub>-2 MTB films (e) with various separation distances. The compressive strain is calculated based on the  $d_{\text{Mo}-\text{Se}}$ , i.e., unit length  $a$ , variations at each atomic column with respect to the  $d_{\text{Mo}-\text{Se}}$  in the monolayer MoSe<sub>2</sub>-1 MTB film (c).

transferred TEM grids were annealed in an ultrahigh vacuum chamber ( $\sim 1 \times 10^{-9}$  Torr) at 180 °C for 10 h prior to STEM characterization to eliminate the surface absorbents.

**STEM-ADF Characterization.** STEM-ADF imaging was carried out on an aberration-corrected JEOL ARM-200F equipped with a cold field emission gun, operating at 60–80 kV (80 kV for MoSe<sub>2</sub> and WSe<sub>2</sub>, 60 kV for MoS<sub>2</sub>). A dwell time of 18  $\mu$ s/pixel was set for single-scan imaging, and 6  $\mu$ s/pixel was set for sequential Z-contrast imaging. Sequential images were aligned by Python scripts to eliminate image drift. In order to improve the accuracy of determining the lattice constant, 10 sequential STEM-ADF images were aligned and stacked by Python scripts to remove lattice distortions induced by the scanning.

**Image Simulation and Analysis.** *Image Simulation.* STEM-ADF image simulations were done by QSTEM. Python scripts were developed for massively calculating the Mo–Mo distances for higher accuracy.

**Distance Calculation.** A Wiener background subtraction filter<sup>32</sup> was applied to remove continuous contributions from amorphous phases. Positions of atomic columns were found by using the Laplacian of Gaussian (LoG) method<sup>33</sup> with subpixel accuracy. Positions within the region of interest are isolated by a ray tracing algorithm. Positions of the topmost row of atomic columns are set to zero, and positions of other rows are determined from the LoG method. The final distance of the same row is averaged and recalculated referring to the predefined topmost row.

**DFT Calculations.** First-principles calculations were performed based on DFT, employing projector-augmented wave pseudopotentials<sup>34</sup> and the Perdew–Burke–Ernzerhof<sup>35</sup> form of the exchange-

correlation functional, as implemented in the Vienna *ab initio* simulation package code.<sup>36</sup> Using van der Waals density functional method,<sup>37,38</sup> the optimized lattice constants of MoSe<sub>2</sub>, WSe<sub>2</sub>, and MoS<sub>2</sub> are 3.295, 3.296, and 3.165 Å, respectively. We employed an energy cutoff of 280 eV for plane waves, and the criterion for total energy convergence was set to 10<sup>-4</sup> eV. All atoms were relaxed during geometry optimization until the magnitude of forces was less than 0.01 eV/Å. Considering the edge effect to the MTBs, the MoSe<sub>2</sub> nanowires we built are 64 Å wide (see Figure 5), representing a  $14\sqrt{3} \times 1$  unit cell.

## ASSOCIATED CONTENT

### S Supporting Information

The Supporting Information is available free of charge on the ACS Publications website at DOI: 10.1021/acsnano.7b09029.

Discussion on the superlattice structure between the MTB and the bulk lattice, quantification of strain, symmetry breaking at the MTB region, and interlayer vdW coupling (PDF)

## AUTHOR INFORMATION

### Corresponding Authors

\*E-mail: wuzhou@ucas.ac.cn.

\*E-mail: chmlohkp@nus.edu.sg.

### ORCID

Xiaoxu Zhao: 0000-0001-9746-3770

Jianyi Chen: 0000-0002-3757-7634  
Kian Ping Loh: 0000-0002-1491-743X

## Author Contributions

X.Z. and Z.D. contributed equally to this work. X.Z., W.Z., and K.P.L. conceived this project. W.Z., K.P.L., and S.J.P. supervised the execution of the whole work. X.Z. did the electron microscopy characterization and image analysis under the supervision of W.Z. and S.J.P. Z.D. did the DFT calculation under the supervision of K.P.L. J.C. and S.M.P. grew the samples. J.D. developed the python script. All the authors discussed the results and participated in writing the manuscript.

## Notes

The authors declare no competing financial interest.

## ACKNOWLEDGMENTS

K.P.L. thanks the MOE Tier 2 grant Porous, Conjugated Molecular Framework for Energy Storage (MOE2016-T2-1-003) and funding by SinBeRISE CREATE, National Research Foundation, Prime Minister's Office. W.Z. acknowledges support from the CAS Key Research Program of Frontier Sciences and the Natural Science Foundation of China (S1622211). S.J.P. thanks the National University of Singapore for funding.

## REFERENCES

- (1) Bertolazzi, S.; Brivio, J.; Kis, A. Stretching and Breaking of Ultrathin MoS<sub>2</sub>. *ACS Nano* **2011**, *5*, 9703–9709.
- (2) McCreary, A.; Ghosh, R.; Amani, M.; Wang, J.; Duerloo, K. A. N.; Sharma, A.; Jarvis, K.; Reed, E. J.; Dongare, A. M.; Banerjee, S. K.; Terrones, M.; Namburu, R. R.; Dubey, M. Effects of Uniaxial and Biaxial Strain on Few-Layered Terrace Structures of MoS<sub>2</sub> Grown by Vapor Transport. *ACS Nano* **2016**, *10*, 3186–3197.
- (3) Castellanos-Gomez, A.; Roldan, R.; Cappelluti, E.; Buscema, M.; Guinea, F.; van der Zant, H. S. J.; Steele, G. A. Local Strain Engineering in Atomically Thin MoS<sub>2</sub>. *Nano Lett.* **2013**, *13*, 5361–5366.
- (4) Conley, H. J.; Wang, B.; Ziegler, J. I.; Haglund, R. F.; Pantelides, S. T.; Bolotin, K. I. Bandgap Engineering of Strained Monolayer and Bilayer MoS<sub>2</sub>. *Nano Lett.* **2013**, *13*, 3626–3630.
- (5) Feng, J.; Qian, X. F.; Huang, C. W.; Li, J. Strain-Engineered Artificial Atom as a Broad-Spectrum Solar Energy Funnel. *Nat. Nat. Photonics* **2012**, *6*, 866–872.
- (6) Quereda, J.; Palacios, J. J.; Agrait, N.; Castellanos-Gomez, A.; Rubio-Bollinger, G. Strain Engineering of Schottky Barriers in Single- and Few-Layer MoS<sub>2</sub> Vertical Devices. *2D Mater.* **2017**, *4*, 021006.
- (7) Ghorbani-Asl, M.; Borini, S.; Kuc, A.; Heine, T. Strain-Dependent Modulation Of Conductivity in Single-Layer Transition-Metal Dichalcogenides. *Phys. Rev. B: Condens. Matter Mater. Phys.* **2013**, *87*, 235434.
- (8) Shen, T. T.; Penumatcha, A. V.; Appenzeller, J. Strain Engineering for Transition Metal Dichalcogenides Based Field Effect Transistors. *ACS Nano* **2016**, *10*, 4712–4718.
- (9) Li, H.; Tsai, C.; Koh, A. L.; Cai, L. L.; Contrynman, A. W.; Frapapane, A. H.; Zhao, J. H.; Han, H. S.; Manoharan, H. C.; Abild-Pedersen, F.; Norskov, J. K.; Zheng, X. L. Activating And Optimizing MoS<sub>2</sub> Basal Planes for Hydrogen Evolution Through the Formation of Strained Sulphur Vacancies. *Nat. Mater.* **2016**, *15*, 48–53.
- (10) Lu, P.; Wu, X. J.; Guo, W. L.; Zeng, X. C. Strain-Dependent Electronic and Magnetic Properties of MoS<sub>2</sub>Monolayer, Bilayer, Nanoribbons and Nanotubes. *Phys. Chem. Chem. Phys.* **2012**, *14*, 13035–13040.
- (11) Wang, Y. L.; Cong, C. X.; Yang, W. H.; Shang, J. Z.; Peimyoo, N.; Chen, Y.; Kang, J. Y.; Wang, J. P.; Huang, W.; Yu, T. Strain-Induced Direct-Indirect Bandgap Transition and Phonon Modulation in Monolayer WS<sub>2</sub>. *Nano Res.* **2015**, *8*, 2562–2572.
- (12) Yun, W. S.; Han, S. W.; Hong, S. C.; Kim, I. G.; Lee, J. D. Thickness and Strain Effects on Electronic Structures of Transition Metal Dichalcogenides: 2H-M X-2 Semiconductors (M = Mo, W; X = S, Se, Te). *Phys. Rev. B: Condens. Matter Mater. Phys.* **2012**, *85*, 033305.
- (13) Scalise, E.; Houssa, M.; Pourtois, G.; Afanas'ev, V. V.; Stesmans, A. Strain-Induced Semiconductor to Metal Transition in The Two-Dimensional Honeycomb Structure Of MoS<sub>2</sub>. *Nano Res.* **2012**, *5* (1), 43–48.
- (14) Wu, W. Z.; Wang, L.; Li, Y. L.; Zhang, F.; Lin, L.; Niu, S. M.; Chenet, D.; Zhang, X.; Hao, Y. F.; Heinz, T. F.; Hone, J.; Wang, Z. L. Piezoelectricity of Single-Atomic-Layer MoS<sub>2</sub> for Energy Conversion and Piezotronics. *Nature* **2014**, *S14*, 470.
- (15) Lin, J. H.; Fang, W. J.; Zhou, W.; Lupini, A. R.; Idrobo, J. C.; Kong, J.; Pennycook, S. J.; Pantelides, S. T. AC/AB Stacking Boundaries in Bilayer Graphene. *Nano Lett.* **2013**, *13*, 3262–3268.
- (16) Alden, J. S.; Tsen, A. W.; Huang, P. Y.; Hovden, R.; Brown, L.; Park, J.; Muller, D. A.; McEuen, P. L. Strain Solitons and Topological Defects in Bilayer Graphene. *Proc. Natl. Acad. Sci. U. S. A.* **2013**, *110*, 11256–60.
- (17) Lee, C.; Wei, X. D.; Kysar, J. W.; Hone, J. Measurement of the Elastic Properties and Intrinsic Strength of Monolayer Graphene. *Science* **2008**, *321*, 385–388.
- (18) Yang, Y. C.; Li, X.; Wen, M. R.; Hacopian, E.; Chen, W. B.; Gong, Y. J.; Zhang, J.; Li, B.; Zhou, W.; Ajayan, P. M.; Chen, Q.; Zhu, T.; Lou, J. Brittle Fracture of 2D MoSe<sub>2</sub>. *Adv. Mater.* **2017**, *29*, 1604201.
- (19) Zhou, W.; Zou, X. L.; Najmaei, S.; Liu, Z.; Shi, Y. M.; Kong, J.; Lou, J.; Ajayan, P. M.; Yakobson, B. I.; Idrobo, J. C. Intrinsic Structural Defects in Monolayer Molybdenum Disulfide. *Nano Lett.* **2013**, *13*, 2615–2622.
- (20) Komsa, H. P.; Krasheninnikov, A. V. Engineering the Electronic Properties of Two-Dimensional Transition Metal Dichalcogenides by Introducing Mirror Twin Boundaries. *Adv. Electron. Mater.* **2017**, *3*, 1600468.
- (21) Zou, X. L.; Yakobson, B. I. Metallic High-Angle Grain Boundaries in Monolayer Polycrystalline WS<sub>2</sub>. *Small* **2015**, *11*, 4503–4507.
- (22) Lin, J. H.; Pantelides, S. T.; Zhou, W. Vacancy-Induced Formation and Growth of Inversion Domains in Transition-Metal Dichalcogenide Monolayer. *ACS Nano* **2015**, *9*, 5189–5197.
- (23) Lehtinen, O.; Komsa, H. P.; Pulkkin, A.; Whitwick, M. B.; Chen, M. W.; Lehnert, T.; Mohn, M. J.; Yazayev, O. V.; Kis, A.; Kaiser, U.; Krasheninnikov, A. V. Atomic Scale Microstructure and Properties of Se-Deficient Two-Dimensional MoSe<sub>2</sub>. *ACS Nano* **2015**, *9*, 3274–3283.
- (24) Hytch, M. J.; Snoeck, E.; Kilaas, R. Quantitative Measurement of Displacement and Strain Fields from HREM Micrographs. *Ultramicroscopy* **1998**, *74*, 131–146.
- (25) Pan, H.; Li, X.; Zhang, F.; Yang, S. Y. A Perfect Valley Filter in a Topological Domain Wall. *Phys. Rev. B: Condens. Matter Mater. Phys.* **2015**, *92*, 041404.
- (26) Pulkkin, A.; Yazayev, O. V. Spin- and Valley-Polarized Transport Across Line Defects in Monolayer MoS<sub>2</sub>. *Phys. Rev. B: Condens. Matter Mater. Phys.* **2016**, *93*, 041419.
- (27) Gunlycke, D.; White, C. T. Graphene Valley Filter Using a Line Defect. *Phys. Rev. Lett.* **2011**, *106*, 136806.
- (28) Bjorkman, T.; Gulans, A.; Krasheninnikov, A. V.; Nieminen, R. M. van der Waals Bonding in Layered Compounds from Advanced Density-Functional First-Principles Calculations. *Phys. Rev. Lett.* **2012**, *108*, 235502.
- (29) Ma, Y. J.; Kolekar, S.; Coy Diaz, H.; Aprojanz, J.; Miccoli, I.; Tegenkamp, C.; Batzill, M. Metallic Twin Grain Boundaries Embedded in MoSe<sub>2</sub>Monolayers Grown by Molecular Beam Epitaxy. *ACS Nano* **2017**, *11*, 5130–5139.
- (30) Chen, J. Y.; Zhao, X. X.; Tan, S. J. R.; Xu, H.; Wu, B.; Liu, B.; Fu, D. Y.; Fu, W.; Geng, D. C.; Liu, Y. P.; Liu, W.; Tang, W.; Li, L. J.; Zhou, W.; Sum, T. C.; Loh, K. P. Chemical Vapor Deposition of Large-Size Monolayer MoSe<sub>2</sub> Crystals on Molten Glass. *J. Am. Chem. Soc.* **2017**, *139*, 1073–1076.

- (31) Regan, W.; Alem, N.; Aleman, B.; Geng, B. S.; Girit, C.; Maserati, L.; Wang, F.; Crommie, M.; Zettl, A. A direct transfer of layer-area graphene. *Appl. Phys. Lett.* **2010**, *96*, 113102.
- (32) Kilaas, R. Optimal and Near-Optimal Filters in High-Resolution Electron Microscopy. *J. Microsc.* **1998**, *190*, 45–51.
- (33) Lindeberg, T. Scale Selection Properties of Generalized Scale-Space Interest Point Detectors. *J. Math. Imaging. Vis.* **2013**, *46*, 177–210.
- (34) Blochl, P. E. Projector Augmented-Wave Method. *Phys. Rev. B: Condens. Matter Mater. Phys.* **1994**, *50*, 17953–17979.
- (35) Perdew, J. P.; Burke, K.; Ernzerhof, M. Generalized Gradient Approximation Made Simple. *Phys. Rev. Lett.* **1996**, *77*, 3865–3868.
- (36) Kresse, G.; Hafner, J. Ab initio Molecular Dynamics for Liquid Metals. *Phys. Rev. B: Condens. Matter Mater. Phys.* **1993**, *47*, 558–561.
- (37) Dion, M.; Rydberg, H.; Schroder, E.; Langreth, D. C.; Lundqvist, B. I. Van der Waals Density Functional For General Geometries. *Phys. Rev. Lett.* **2004**, *92*, 246401.
- (38) Klimes, J.; Bowler, D. R.; Michaelides, A. Chemical Accuracy for the Van der Waals Density Functional. *J. Phys.: Condens. Matter* **2010**, *22*, 022201.